(Received 31 December 2025, Accepted 22 January 2026, Scheduled 13 February 2026)

A Miniaturized Wideband PIFA Antenna for Medical Implant Systems

Amina Abbas[1], Farid Bouttout[1], Asma Djellid[2], Youcef Braham Chaouche[3,*], Ismail Benmabrouk[4], and Amjad Iqbal[4]

[1] *Laboratory of Advanced Electronics and Telecommunications (LEAT), Department of Electronics Faculty of Science and Technology, University of Bordj Bou Arreridj, El-Anasser 34030, BBA, Algeria*
[2] *Electrical Engineering Laboratory, Department of Electronic, Faculty of Technology, University of M'sila, M'sila, Algeria*
[3] *Underground Communications Research Laboratory, Engineering School University of Quebec at Abitibi-Temiscamingue (UQAT), Val d'Or, QC J9P 1Y3, Canada*
[3] *Department of Engineering, Durham University, Durham DH1 3LE, UK*

ABSTRACT: This article presents a miniaturized wideband planar inverted-F antenna (PIFA) for deep biomedical implant applications at 915 MHz. Compactness and wide impedance bandwidth are achieved using a shorting pin, a circular radiating patch, and open-ended slots etched in the ground plane. The antenna occupies an ultra-small volume of 63.5 mm^3 and is designed and analyzed inside a four-layer cylindrical human tissue phantom. The simulated and measured results show stable impedance matching over the ISM band, with a measured −10 dB bandwidth of 481 MHz (44.02%) and a peak realized gain of −28 dBi. Specific absorption rate (SAR) analysis confirms compliance with IEEE safety limits. In-vitro measurements using minced pork show close agreement with simulations, validating the antenna's performance and its suitability for reliable deep biomedical implant communication systems.

1. INTRODUCTION

Biomedical applications have experienced significant advancements over recent decades, driven by continuous progress in modern communication and sensing technologies [1]. Implantable biomedical devices (IMDs) play a vital role in a wide range of medical applications, including targeted hyperthermia for cancer treatment, remote-controlled drug delivery, and continuous monitoring of physiological parameters [2, 3]. These devices acquire physiological data from the human body and enable wireless communication with external monitoring systems through embedded implantable antennas [4]. An overview of an implantable antenna system is illustrated in Fig. 1.

Unlike conventional free-space antennas, implantable antennas operate in a highly lossy, inhomogeneous, and dispersive environment [5]. Their radiation characteristics are strongly affected by the electromagnetic properties of surrounding biological tissues [6]. The human body consists of multiple tissue layers, such as skin, fat, blood, and bone, each exhibiting distinct dielectric properties. This complexity imposes significant challenges in the design of compact, efficient, and biocompatible antennas for implantable medical applications [7].

Several frequency bands have been allocated for wireless communication in implantable medical systems. The MedRadio band (401–406 MHz) and industrial, scientific, and medical (ISM) bands at 900 MHz and 2.4 GHz are among the most commonly used. Lower frequency bands offer improved signal penetration and reduced propagation losses within the human body; however, they impose strict constraints on radiated power and antenna miniaturization, limiting achievable bandwidth and radiation efficiency [8].

FIGURE 1. An overview of an implantable antenna system.

Designing antennas for deeply implanted biomedical devices, such as wireless capsule endoscopes, remains particularly challenging. As these devices traverse complex biological environments, variations in tissue composition and dielectric properties significantly influence antenna performance and communication reliability [9]. Consequently, extensive research efforts have been devoted to developing implantable antennas capable of maintaining stable performance under such dynamic conditions.

Several implantable antenna designs operating in the 915 MHz ISM band have been investigated for biomedical telemetry and implantable medical device applications. Due

* Corresponding author: Youcef Braham Chaouche (bray02@uqat.ca).

to the highly lossy and dispersive nature of human tissues, implantable antennas are subject to fundamental limitations in terms of radiation efficiency and achievable power density, which have been thoroughly analyzed to guide in-body antenna design [10]. Miniaturized dual-band and wideband implantable antennas covering the 915 MHz ISM band have been reported for gastrointestinal and leadless biomedical applications, demonstrating enhanced impedance stability in lossy tissue environments [11]. In addition, self-duplexing implantable antennas have been introduced to improve communication reliability and system integration in capsule-based devices [12]. Conformal and monopole-based implantable antennas operating at 915 MHz have also been proposed, offering compact geometries but often at the expense of limited bandwidth [13]. Circularly polarized implantable antennas operating at 915 MHz have been reported to improve orientation robustness and communication reliability; however, these designs often suffer from a limited impedance bandwidth, relatively large physical size, or elevated specific absorption rate (SAR) values [14].

Despite these advances, existing implantable antenna designs still involve trade-offs among compactness, impedance bandwidth, radiation efficiency, and SAR constraints, which limit their seamless integration into next-generation implantable medical devices. Therefore, further research is required to develop implantable antennas that simultaneously achieve compact size, wide bandwidth, acceptable gain, reduced SAR, and reliable telemetry performance for deep implantation scenarios.

In this context, this article presents a compact wideband implantable antenna operating in the 915 MHz ISM band for deeply implanted biomedical devices, such as wireless capsule endoscopes and leadless pacemakers. The proposed antenna occupies a compact volume of $10 \times 10 \times 1.27$ mm^3 and achieves a wide operational bandwidth of 481 MHz (852–1333 MHz) with a simulated peak gain of -28 dBi. Prototype fabrication and experimental validation confirm good agreement between simulated and measured results. A comparative performance analysis with previously reported implantable antennas is provided in Table 3, highlighting the proposed design's advantages in terms of compactness, bandwidth, gain, and SAR compliance.

The remainder of this paper is organized as follows. Section 2 describes the antenna configuration and design methodology. Section 3 presents the parametric analysis and performance evaluation. Section 4 discusses the experimental results and link budget analysis. Finally, Section 5 concludes the paper.

2. ANTENNA STRUCTURE AND HUMAN BODY MODEL

Figure 2 shows the geometry of the proposed compact, wideband antenna designed for medical applications. Specifically, Fig. 2(a) is the front view (depicting the radiating element), Fig. 2(b) the rear view (showing the ground plane), and Fig. 2(c) the lateral and exploded views (illustrating the layer positioning).

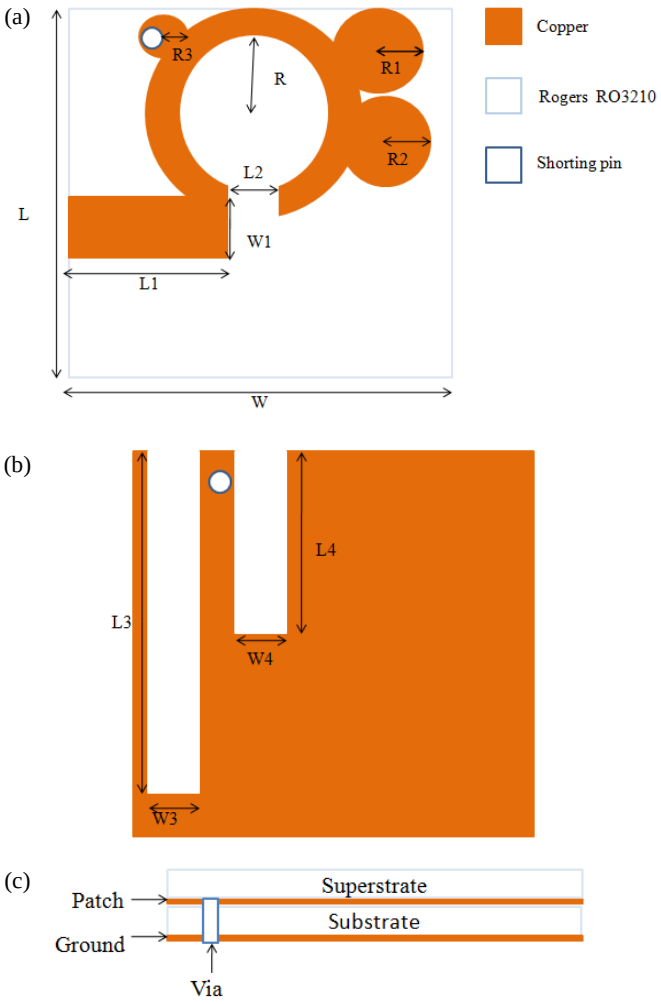

FIGURE 2. Geometrical structure of the proposed PIFA antenna: (a) front view, (b) back view, and (c) side view.

The antenna has a key-shaped radiating element sandwiched between a substrate and a superstrate. Both the substrate and superstrate are made of Rogers RO3210 dielectric (relative permittivity $\epsilon_r = 10.2$, loss tangent $\tan\delta = 0.003$). Each dielectric layer has a thickness of 0.635 mm. The substrate and superstrate materials have been widely used in biomedical antenna studies due to their stable dielectric properties and compatibility with standard biocompatible encapsulation materials. The superstrate layer further isolates the radiating element from the surrounding tissues, thereby making the proposed design suitable for long-term implantable applications. The overall antenna measures $10 \times 10 \times 1.27$ mm^3, yielding a total volume of approximately 63.5 mm^3.

The excitation is provided by a microstrip line feed consisting of a rectangular strip of width $W1$ and length $L1$. Additionally, a short-circuit via (diameter 0.6 mm) is strategically placed based on parametric studies to aid in miniaturization and improve impedance matching.

The antenna design was achieved through a systematic multistep optimization process based on extensive parametric studies involving geometrical dimensions and element positioning. Both the radiating patch and the ground plane were progres-

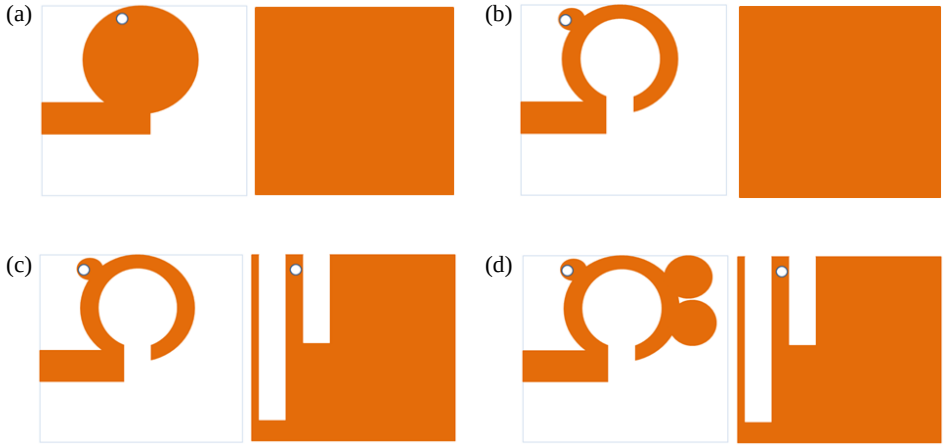

FIGURE 3. Evolution prototypes of the proposed antenna: (a) Step 1, (b) Step 2, (c) Step 3, and (d) Step 4.

sively modified by introducing slots and conductive tracks of various shapes to control the resonant frequency, impedance matching, and bandwidth. The design evolution consists of four main steps, each highlighting the functional contribution of specific structural modifications, as summarized below.

Step 1: The initial configuration consisted of a conventional planar inverted-F antenna (PIFA) with a full ground plane. The antenna was excited using a microstrip line feed with dimensions of 1.5 mm $\times$ 5.5 mm. A circular radiating patch with a radius of 3 mm was employed, and a short-circuit pin connected the patch to the ground plane, as shown in Fig. 3(a). This preliminary design exhibited a weak resonance with a reflection coefficient of -9.2 dB at 2.1 GHz, indicating inadequate impedance matching and a resonance frequency far from the targeted band.

Step 2: In the second step, a circular conductive track was introduced to optimize the placement of the short-circuit pin. Additionally, a circular slit with a radius of 2 mm was etched at the center of the radiating patch. The feed line length was reduced to $L1$, and a rectangular slot of 1 mm $\times$ 1 mm was added near the feed region. These modifications transformed the radiating element into an arc-shaped structure, as illustrated in Fig. 3(b). As a result, the resonance frequency shifted from 2.1 GHz to 1.88 GHz, with a significant improvement in impedance matching, reaching -27.2 dB.

Step 3: To further reduce the operating frequency, additional modifications were applied to the ground plane. Two rectangular slots were introduced near the short-circuit pin, as depicted in Fig. 3(c). The slots have lengths $L3$ and $L4$ and identical widths $W3$ and $W4$. These changes effectively shifted the resonance frequency down to 1.08 GHz. However, the impedance matching deteriorated at this stage, necessitating further optimization.

Step 4: In the final design stage, two circular slits with radius $R1$ were etched into the radiating patch to achieve the targeted resonance frequency with improved impedance matching. The final antenna configuration, shown in Fig. 3(d), exhibits excellent matching performance at the desired operating band, as confirmed by the reflection coefficient results presented in Fig. 5.

The wide impedance bandwidth achieved by the proposed antenna results from the combined electromagnetic effects of the modified radiating patch and the slotted ground plane. The introduction of slits in the radiating patch effectively increases the electrical length of the antenna by elongating the surface current paths, which shifts the fundamental resonance toward lower frequencies and contributes to miniaturization. In addition, these slits enable the excitation of multiple closely spaced resonant modes.

The slots etched in the ground plane further perturb the current distribution and introduce additional coupling paths between the patch and the ground. This interaction modifies the input impedance and improves impedance matching over a wider frequency range. As a result, the resonant modes generated by the patch slits and ground slots overlap, leading to a broadband impedance response. The cooperative effect of these structural features is responsible for the wide bandwidth observed in the proposed design. The final optimized parameters are summarized in Table 1.

TABLE 1. Parameters of the designed antenna.

(a) Length parameters (mm)

Parameter	L	$L1$	$L2$	$L3$	$L4$
Value	10	4.5	1	9	5

(b) Width and Radius parameters (mm)

Parameter	W	$W1$	$W3$	$W4$	R	$R1$	$R2$	$R3$
Value	10	1.5	1	1	2	1.1	1.1	0.3

3. STRUCTURE OF THE HUMAN BODY MODEL

Antenna simulations were performed using Ansys HFSS. A four-layer cylindrical human arm phantom, consisting of skin, fat, muscle, and bone tissues, was employed in the simulation environment. The antenna was implanted within the muscle layer at a depth of 10 mm beneath the skin surface, as illus-

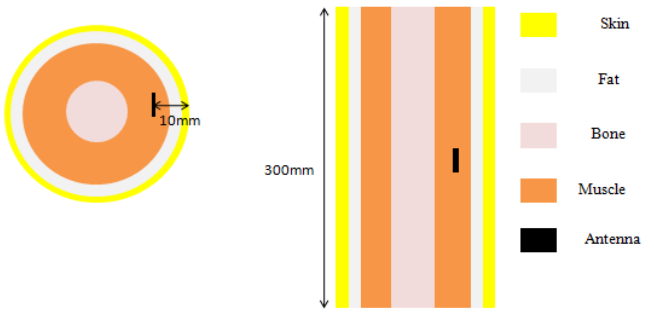

FIGURE 4. Structure of the implant environment.

trated in Fig. 4. This implantation depth was selected based on the parametric analysis presented in the following section, which demonstrates its optimal impact on impedance matching and resonance behavior. The geometrical dimensions and dielectric properties of each tissue layer are summarized in Table 2.

TABLE 2. Dimensions and dielectric characteristics of biological tissues at 915 MHz [15].

Biological Tissue	Skin	Fat	Muscle	Bone
ε_r	41.329	5.4596	54.997	12.44
σ (S/m)	0.8716	0.05140	0.9480	0.1451
Thickness (mm)	2.5	2	25	22.5

4. RESULTS AND DISCUSSION

4.1. Analysis of Simulation Results

This section presents a parametric analysis of the proposed antenna to evaluate the influence of surrounding biological tissues and implantation depth on its performance.

4.1.1. Effect of Surrounding Tissue

For the analysis of different biological tissues, a homogeneous single-layer cylindrical phantom was employed, as shown in Fig. 5. In this configuration, the dielectric properties of the cylinder were individually assigned to represent muscle, skin, bone, and fat tissues. This simplified model was adopted to isolate the individual contribution of each tissue to the antenna resonance and impedance matching, without the influence of tissue interfaces. High-permittivity tissues (muscle and skin) produce a downward shift of the resonant frequency and provide good impedance matching, with S_{11} minima below -29 dB. In contrast, low-permittivity fat yields an upward shift of the resonant frequency and a significant degradation of matching ($S_{11} \approx -3.02$ dB). Bone exhibits an intermediate behavior. Overall, the resonance ordering follows $f_{\text{muscle}} < f_{\text{skin}} < f_{\text{bone}} < f_{\text{fat}}$, which is consistent with dielectric-loading theory. The final antenna performance was evaluated using a four-layer cylindrical model (skin-fat-muscle-bone). This multilayer configuration accounts for tissue interfaces and combined dielectric loading, providing a more realistic representation of in-

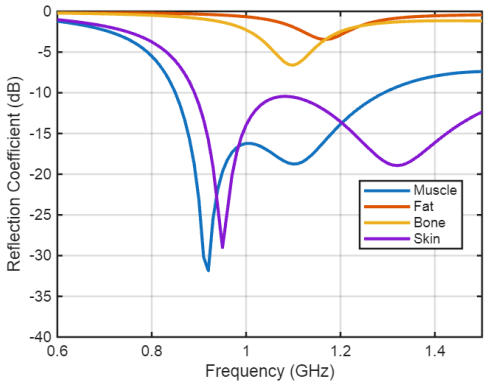

FIGURE 5. Reflection coefficient of the implantable antenna for different surrounding tissues using a homogeneous single-layer cylindrical model.

body conditions and improving the relevance of the obtained results.

4.1.2. Effect of Implantation Depth (ID)

Figure 6 shows a parametric analysis of the implantation depth conducted using a four-layer cylindrical tissue model (skin-fat-muscle-bone). The results show that increasing the implantation depth from 3 mm to 10 mm leads to a progressive downward shift of the resonant frequency and a significant improvement in impedance matching. At shallow depth (3 mm), the antenna is strongly affected by superficial tissue interfaces, resulting in a higher resonant frequency. As the antenna is placed deeper inside the body, it experiences stronger and more homogeneous dielectric loading from muscle tissue. At 10 mm depth, the antenna resonates at 915 MHz with a minimum reflection coefficient of -51.7 dB, indicating excellent impedance matching within the target ISM band. At this depth, the antenna is primarily surrounded by muscle tissue, resulting in strong and homogeneous dielectric loading. This condition is representative of practical biomedical implants, such as capsule endoscopes and leadless devices, and provides a realistic and conservative scenario for evaluating antenna performance in lossy biological environments. Reliable telemetry performance in deep implantable applications depends on the combined effects of impedance matching, radiation efficiency, propagation dis-

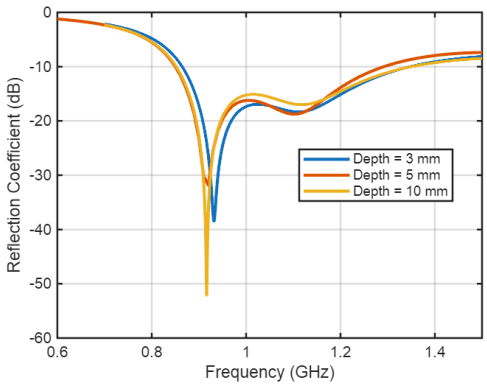

FIGURE 6. Effect of implantation depth on the reflection coefficient of the implantable antenna using the four-layer cylindrical tissue model.

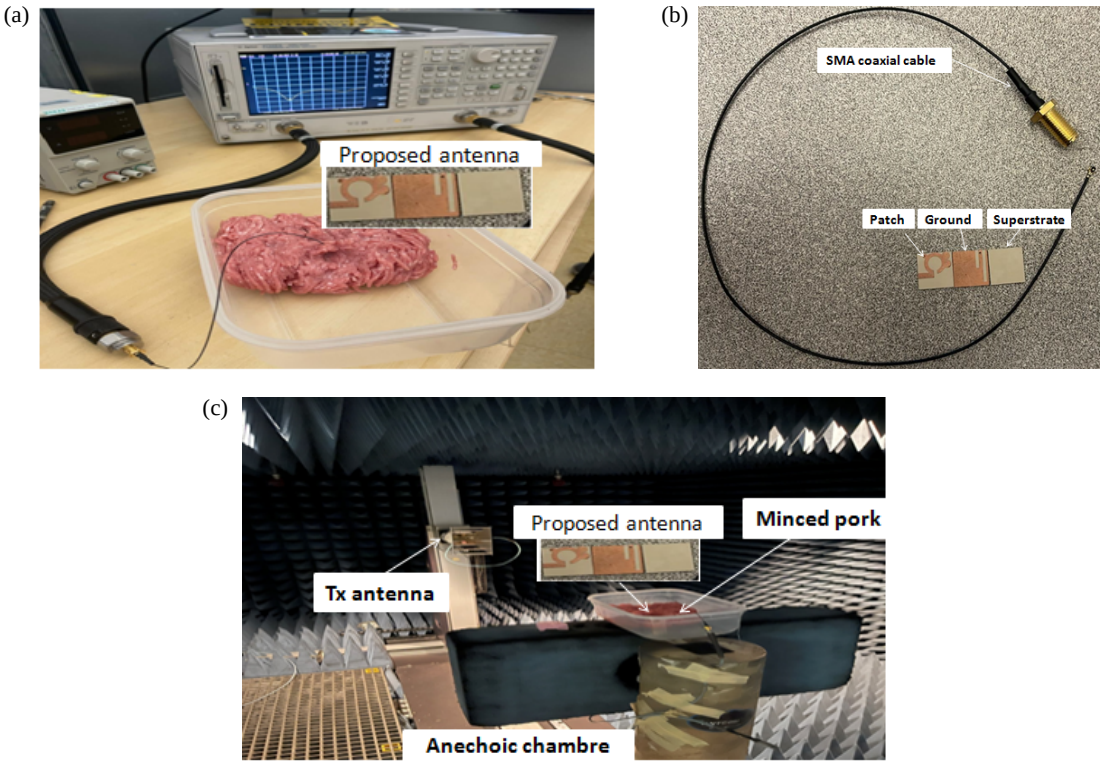

FIGURE 7. Fabricated prototype and measurement setup: (a) fabricated antenna, (b) reflection coefficient measurement, and (c) gain measurement.

tance, and receiver sensitivity. In practical biomedical telemetry systems, the communication distance between the implanted device and external reader is typically limited to a few centimeters. At such short ranges, the propagation loss is significantly reduced, allowing sufficient received signal strength despite the strong attenuation caused by surrounding biological tissues. Moreover, the wide impedance bandwidth of the proposed antenna ensures stable matching under varying implantation conditions, which contributes to consistent power transfer and improved link robustness. When combined with low-noise external receivers and modern digital modulation techniques commonly employed in implantable medical devices, the proposed antenna is capable of supporting reliable short-range wireless communication for deep biomedical implantation scenarios.

4.2. Antenna Fabrication and Measurements

In the preceding section, a miniaturized planar inverted-F antenna (PIFA) was designed and optimized for implantable biomedical applications. To validate the simulation results, a prototype of the proposed antenna was fabricated and experimentally characterized, as shown in Fig. 7. For in vitro measurements, the antenna was embedded in minced pork, which serves as a practical surrogate for the multilayer human tissue model employed in the simulations [16]. This measurement setup was adopted to approximate the dielectric properties of human tissues under realistic implantation conditions.

4.3. Return Loss

Figure 8 presents a comparison between the simulated and measured reflection coefficients of the proposed antenna. When the fabricated prototype is embedded in minced pork, a slight downward shift in the resonance frequency is observed, with the measured resonance occurring at 832 MHz. In addition, the operating bandwidth becomes wider. The measured -10 dB impedance bandwidth is 481 MHz, extending from 852 MHz to 1333 MHz, which corresponds to 44.02% fractional bandwidth and fully covers the 915 MHz ISM band.

The discrepancies between simulated and measured results can be attributed to several factors. First, the soldering process may slightly modify the antenna geometry, leading to variations in the resonant behavior. Second, due to the miniature size of the antenna, mechanical compression or deformation may oc-

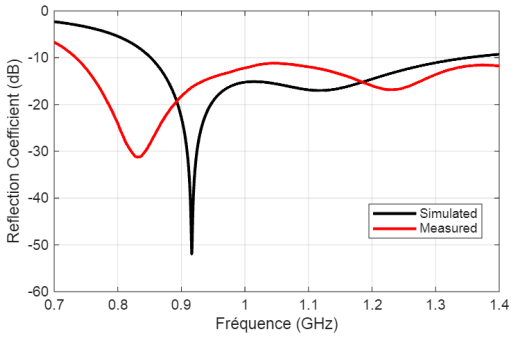

FIGURE 8. Comparison of simulated and measured reflection coefficients (S_{11}).

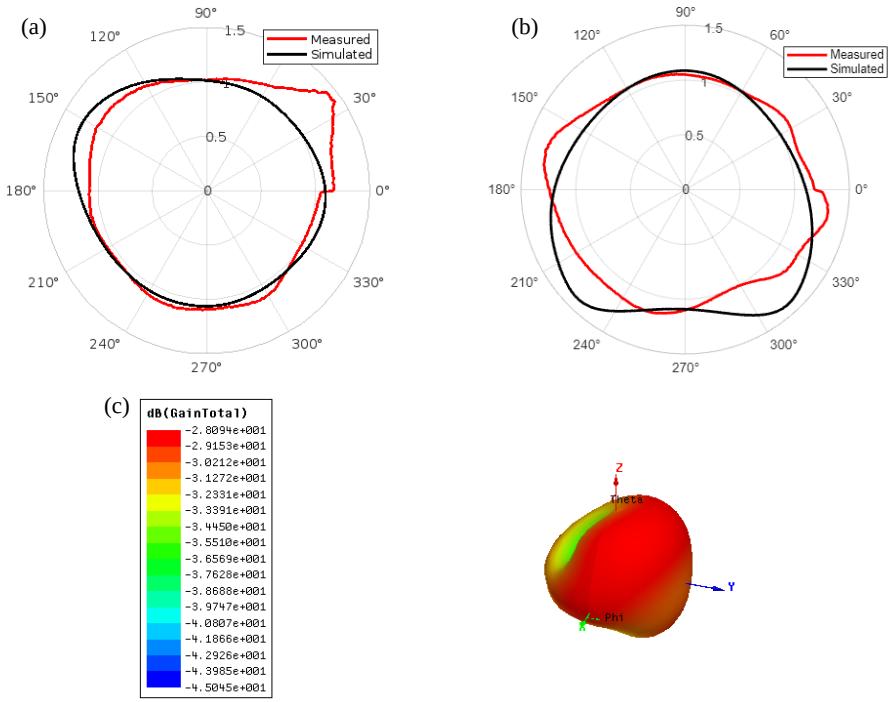

FIGURE 9. Simulated and measured radiation pattern: (a) E-plane, (b) H-plane, and (c) 3D plan.

cur during implantation into the pork tissue, affecting the measured response. Third, fabrication tolerances, including the replacement of the short-circuit pin with a metallized via hole, as well as environmental conditions during measurements, may introduce additional deviations.

Despite these minor differences, the measured and simulated results exhibit consistent resonance characteristics. The wide impedance bandwidth achieved by the proposed antenna effectively covers the ISM 915 MHz band, thereby confirming its suitability for implantable biomedical communication applications. The intended operating band of the proposed antenna is the 915 MHz ISM band. The wide bandwidth provides robustness against detuning effects caused by tissue heterogeneity, implantation depth variations, and fabrication tolerances, ensuring stable operation in realistic implantable scenarios.

4.4. Radiaton Pattern

Radiation pattern measurements were carried out inside an anechoic chamber, as shown in Fig. 7(c). The proposed antenna exhibits quasi-omnidirectional radiation characteristics in the E-plane at $\theta = 0°$, and in the H-plane at $\theta = 90°$, as illustrated in Fig. 9. A good agreement between simulated and measured radiation patterns is observed.

Minor discrepancies can be attributed to the electrically small size of the antenna and the inherent difficulty of precise positioning during the measurement process. In addition, coupling mismatch and alignment limitations associated with the horn antenna used in the measurement setup may contribute to measurement inaccuracies. The simulated three-dimensional radiation pattern of the proposed antenna, shown in Fig. 9(c), indicates a maximum realized gain of -28 dBi. The obtained radiation characteristics are consistent with those typically observed for antennas operating in deeply implanted and highly lossy biological environments. In such scenarios, electromagnetic waves experience strong attenuation due to tissue absorption and scattering, which inherently limits radiation efficiency. However, for implantable telemetry applications, communication reliability is governed primarily by the overall link budget rather than antenna gain alone [17]. Given that the separation between the implant and the external reader is generally confined to a few centimeters, the resulting propagation loss remains moderate, enabling adequate received signal strength. In addition, the wide impedance bandwidth of the proposed antenna ensures stable matching and efficient power transfer over the operating band, further enhancing link robustness. When being combined with low-noise external receivers and modern modulation schemes commonly employed in biomedical telemetry systems, the antenna is capable of supporting reliable short-range wireless communication. Comparable radiation performance has been reported in prior implantable antenna studies that successfully demonstrate effective data transmission in the ISM band under similar implantation conditions.

4.5. Current Distribution

The surface current distribution plays a key role in determining the radiation characteristics of the antenna. Fig. 10 illustrates the simulated current distribution of the proposed design at the operating frequency. As shown in Fig. 10(a), strong current concentrations are observed along the left side of the radiating patch and in the vicinity of the short-circuit pin. Similarly, Fig. 10(b) indicates that the surface currents on the ground plane are mainly localized around the etched slots. These current paths confirm the role of the shorting element and slot structures in achieving antenna miniaturization and resonance control.

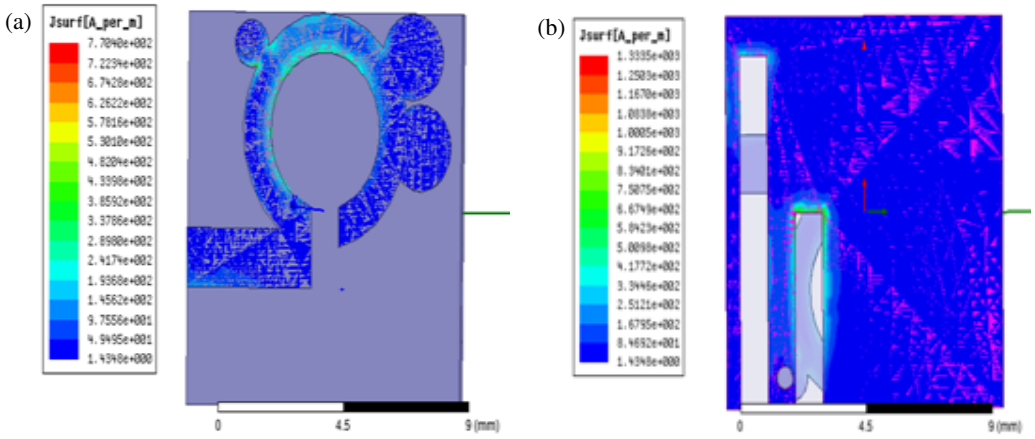

FIGURE 10. surface current distribution: (a) patch and (b) ground.

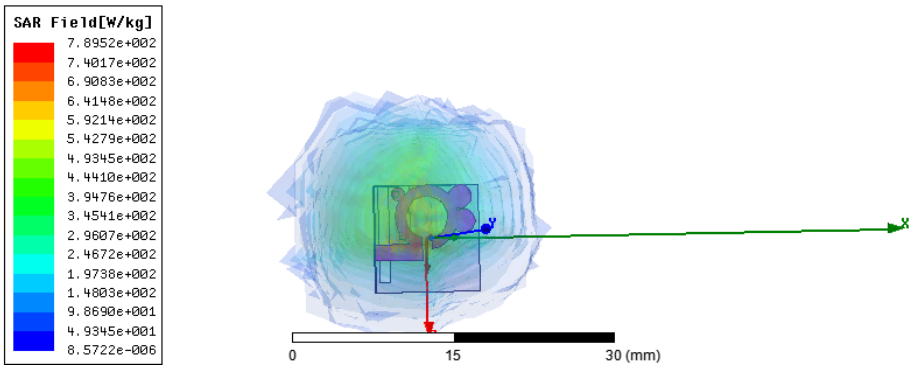

FIGURE 11. SAR distribution within the cylindrical phantom at 915 MHz.

4.6. SAR Analysis

Since the proposed antenna operates in close proximity to biological tissues, an evaluation of the electromagnetic power absorbed by the surrounding tissues is required. This absorption is quantified using the Specific Absorption Rate (SAR). The SAR level is determined from Eq. (1), where σ is the conductivity of the tissue in S/m, E is the electric field in V/m, and ρ is the mass density of the tissue in kg/m^3.

$$\mathrm{SAR} = \frac{\sigma |E|^2}{\rho} \tag{1}$$

According to IEEE safety guidelines, the SAR limits are 2 W/kg averaged over 10 g of tissue and 1.6 W/kg averaged over 1 g of tissue [18]. The SAR distribution of the proposed antenna was evaluated using the four-layer human tissue model. The SAR levels are evaluated using a 1 g averaging mass in the surrounding biological tissues of the implantable antenna. The peak 1 g SAR value of 789 W/kg is obtained at 915 MHz for a normalized accepted input power of 1 W, as illustrated in Fig. 11. Most implantable medical devices operate at very low power levels, typically in the µW-mW range. To satisfy the IEEE/FCC SAR limit of 1.6 W/kg (1 g), the maximum allowable accepted input power of the proposed antenna is 2.03 mW. At a representative implantable operating power of 0.5 mW, the corresponding SAR value scales to 0.395 W/kg, which is above the limit. Therefore, the proposed implantable antenna operates safely within the established SAR constraints.

$$\mathrm{SAR}_{0.5\,\mathrm{mW}} = \mathrm{SAR}_{1\,\mathrm{W}} \times \frac{0.5\,\mathrm{mW}}{1\,\mathrm{W}} = 0.395\,\mathrm{W/kg} \tag{2}$$

$$P_{\max} = \frac{1.6}{789} = 2.03\,\mathrm{mW} \tag{3}$$

5. COMPARATIVE ANALYSIS WITH LITERATURE

Table 3 compares the proposed implantable antenna with recently reported designs operating in the ISM bands. Most existing implantable antennas at 915 MHz suffer from a limited impedance bandwidth, typically below 20%, even when relatively large antenna volumes are used [14, 19–21]. Although multiband and wideband solutions have been reported [23–26], the achieved bandwidth at the fundamental ISM band remains restricted.

In contrast, the proposed antenna achieves a very wide impedance bandwidth of 44.02% at 915 MHz while maintaining a compact volume of only 63.5 mm^3, which represents a favorable size-andwidth tradeoff compared with state-of-the-art designs [23, 24]. This wide bandwidth significantly improves robustness against detuning effects caused by tissue

TABLE 3. Comparison of the antenna performance with existing designs.

Ref	Volume (mm^3)	Frequency (GHz)	BW (%)	Gain (dB)	SAR (1 g)
[14] 2018	153.67	0.915	3.8	−29	–
[19] 2020	285.75	0.915	10.6	−27	517
[20] 2019	284.48	0.402	8.4	−35.9	293.7
		0.915	5.7	−24.3	–
[21] 2022	170.77	0.403	18.4	−41.3	259.5
		0.915	18.5	−23.5	363.2
		2.45	31.2	−28.7	238.1
[22] 2025	24.5	0.915	20	−24	440
		1.470	15	−21	351
[23] 2023	58.9	0.915	10	−27	351
		2.45	9	−18	228
[24] 2021	9.4	0.915	10	−24	331
		1.470	7	−18	241
[25] 2022	12.95	0.915	14	−27.2	377.6
		1.9	24	−22.2	275.4
		2.45	12	−19.9	279.5
[26] 2024	28.81	0.915	23.6	−35.85	41.2
		2.45	12.14	−31.6	43.2
Proposed	**63.5**	**0.915**	**44.02**	**−28**	**789**

heterogeneity and implantation conditions. In terms of radiation performance, the achieved gain of −28 dBi is comparable to that of other implantable antennas operating at the same frequency band [14, 21], despite the reduced antenna size. Moreover, the $SAR_{1\,g}$ value of the proposed antenna remains within acceptable limits under controlled input power conditions and falls within the range of values reported for state-of-the-art implantable antennas [19, 22], confirming its suitability for biomedical implant applications.

Overall, the proposed antenna offers a balanced combination of compact size, ultra-wide bandwidth, acceptable gain, and compliant SAR performance, making it a strong candidate for reliable implantable wireless communication systems.

6. CONCLUSION

A miniaturized implantable antenna operating in the 915 MHz ISM band has been presented. The proposed design employs a complex-shaped radiating structure combined with a shorting pin and a high-permittivity Rogers 3210 substrate to achieve significant miniaturization. The antenna exhibits a wide −10 dB impedance bandwidth of 481 MHz with good impedance matching and a realized gain of −28 dBi. Specific absorption rate (SAR) analysis confirms compliance with established safety standards for biomedical implant applications. To validate the numerical results, a prototype was fabricated and experimentally evaluated using minced pork as a tissue-equivalent medium. The measured results show good agreement with simulations, demonstrating the suitability of the proposed antenna for implantable biomedical communication systems.

REFERENCES

[1] Basir, A., Y. Cho, I. A. Shah, S. Hayat, S. Ullah, M. Zada, S. A. A. Shah, and H. Yoo, "Implantable and ingestible antenna systems: From imagination to realization [bioelectromagnetics]," *IEEE Antennas and Propagation Magazine*, Vol. 65, No. 5, 70–83, Oct. 2023.

[2] Ayesha, A., T. Kalsoom, M. Ur-Rehman, N. Ramzan, S. Karim, and Q. H. Abbasi, "Design and study of a small implantable antenna design for blood glucose monitoring," *The Applied Computational Electromagnetics Society Journal (ACES)*, Vol. 33, No. 10, 1146–1151, 2018.

[3] Malik, N. A., P. Sant, T. Ajmal, and M. Ur-Rehman, "Implantable antennas for bio-medical applications," *IEEE Journal of Electromagnetics, RF and Microwaves in Medicine and Biology*, Vol. 5, No. 1, 84–96, 2021.

[4] Bahrami, H., S. A. Mirbozorgi, R. Ameli, L. A. Rusch, and B. Gosselin, "Flexible, polarization-diverse UWB antennas for implantable neural recording systems," *IEEE Transactions on Biomedical Circuits and Systems*, Vol. 10, No. 1, 38–48, 2016.

[5] Abbas, A., F. Bouttout, A. Djellid, Y. B. Chaouche, and M. Nedil, "Compact antenna for biotelemetry applications in MICS band," in *2025 IEEE International Symposium on Antennas and Propagation and North American Radio Science Meeting (AP-S/CNC-USNC-URSI)*, 682–685, Ottawa, ON, Canada, 2025.

[6] Yousaf, M., I. B. Mabrouk, M. Zada, A. Akram, Y. Amin, M. Nedil, and H. Yoo, "An ultra-miniaturized antenna with ultra-wide bandwidth characteristics for medical implant systems," *IEEE Access*, Vol. 9, 40 086–40 097, 2021.

[7] Ahmad, S., B. Manzoor, K. N. Paracha, S. Haider, M. Liaqat, A. J. A. Al-Gburi, A. Ghaffar, M. Alibakhshikenari, and M. Dalarsson, "A wideband bear-shaped compact size implantable antenna for in-body communications," *Applied Sci-*

ences, Vol. 12, No. 6, 2859, 2022.

[8] Faisal, F. and H. Yoo, "A miniaturized novel-shape dual-band antenna for implantable applications," *IEEE Transactions on Antennas and Propagation*, Vol. 67, No. 2, 774–783, 2019.

[9] Cil, E., S. Dumanli, and D. Nikolayev, "Examination of impedance response of capsule-integrated antennas through gastrointestinal tract," in *2022 16th European Conference on Antennas and Propagation (EuCAP)*, 1–5, Madrid, Spain, 2022.

[10] Bosiljevac, M., A. K. Skrivervik, and Z. Sipus, "In-body antennas design based on fundamental limits of obtainable power density," in *2021 15th European Conference on Antennas and Propagation (EuCAP)*, 1–5, Dusseldorf, Germany, 2021.

[11] Lamkaddem, A., A. E. Yousfi, V. González-Posadas, and D. Segovia-Vargas, "Miniaturized dual band implantable antenna for implanted biomedical devices," *IEEE Access*, Vol. 12, 15 026–15 036, 2024.

[12] Un Noor, S. M., S. A. A. Shah, I. A. Shah, S. Khan, J. Nasir, S. Koziel, and Q. H. Abbasi, "A highly miniaturized circularly polarized self-duplexing implantable antenna with enhanced performance for wireless capsule endoscopy applications," *Scientific Reports*, Vol. 15, No. 1, 35470, 2025.

[13] Alrawashdeh, R., "A dual-band conformal implantable monopole antenna for the 915 MHz and 2.45 GHz ISM bands," *International Journal of Engineering Trends and Technology (IJETT)*, Vol. 73, No. 9, 10–19, 2025.

[14] Liu, C., Y. Zhang, and X. Liu, "Circularly polarized implantable antenna for 915 MHz ISM-band far-field wireless power transmission," *IEEE Antennas and Wireless Propagation Letters*, Vol. 17, No. 3, 373–376, 2018.

[15] Sasaki, K., E. Porter, E. A. Rashed, L. Farrugia, and G. Schmid, "Measurement and image-based estimation of dielectric properties of biological tissues — past, present, and future," *Physics in Medicine & Biology*, Vol. 67, No. 14, 14TR01, 2022.

[16] Alshammari, A., A. Basir, M. Zada, S. A. A. Shah, A. Iqbal, and I. B. Mabrouk, "Miniaturized duplex implantable antenna for wireless data communication and power transfer," *IEEE Open Journal of Antennas and Propagation*, Vol. 6, No. 6, 2062–2073, 2025.

[17] Alazemi, A. J. and A. Iqbal, "A compact and wideband mimo antenna for high-data-rate biomedical ingestible capsules," *Scientific Reports*, Vol. 12, No. 1, 14290, Aug. 2022.

[18] Chaouche, Y. B., M. Nedil, I. B. Mabrouk, and O. M. Ramahi, "A wearable circularly polarized antenna backed by AMC reflector for WBAN communications," *IEEE Access*, Vol. 10, 12 838–12 852, 2022.

[19] Xia, Z., H. Li, Z. Lee, S. Xiao, W. Shao, X. Ding, and X. Yang, "A wideband circularly polarized implantable patch antenna for ISM band biomedical applications," *IEEE Transactions on Antennas and Propagation*, Vol. 68, No. 3, 2399–2404, 2020.

[20] Bakogianni, S. and S. Koulouridis, "A dual-band implantable rectenna for wireless data and power support at sub-GHz region," *IEEE Transactions on Antennas and Propagation*, Vol. 67, No. 11, 6800–6810, Nov. 2019.

[21] Fan, Y., Z. Li, X. Liu, X. Li, C. Xu, and H. Yang, "Compact triple-broadband implantable antenna for multi-functions in telemedicine," *IET Microwaves, Antennas & Propagation*, Vol. 16, No. 2–3, 153–162, 2022.

[22] Lamkaddem, A., A. E. Yousfi, Y. Huang, V. G. Posadas, and D. Segovia-Vargas, "Miniaturized wireless power transfer system with a dual-band implantable antenna for multifunctional biomedical devices," *IEEE Sensors Journal*, Vol. 25, No. 16, 31 473–31 488, Aug. 2025.

[23] Zada, M., I. A. Shah, J. Nasir, A. Basir, and H. Yoo, "Empowering remote patient monitoring with a dual-band implantable rectenna system for wireless power and data transfer," *IEEE Transactions on Antennas and Propagation*, Vol. 71, No. 12, 9509–9522, Dec. 2023.

[24] Iqbal, A., M. Al-Hasan, I. B. Mabrouk, A. Basir, M. Nedil, and H. Yoo, "Biotelemetry and wireless powering of biomedical implants using a rectifier integrated self-diplexing implantable antenna," *IEEE Transactions on Microwave Theory and Techniques*, Vol. 69, No. 7, 3438–3451, Jul. 2021.

[25] Shah, S. M. A., M. Zada, J. Nasir, Owais, and H. Yoo, "Ultra-miniaturized triband antenna with reduced sar for skin and deep tissue implants," *IEEE Transactions on Antennas and Propagation*, Vol. 70, No. 9, 8518–8529, Sep. 2022.

[26] Iqbal, A., S. H. Kiani, M. Al-Hasan, I. B. Mabrouk, and T. A. Denidni, "A compact dual-band implantable MIMO antenna for wireless capsule endoscopy," *IEEE Transactions on Antennas and Propagation*, Vol. 72, No. 10, 7515–7524, Oct. 2024.